Letter Vol. 44, No. 4 / 15 February 2019 / Optics Letters 927

Optics Letters

Three-dimensional metacrystals with a broadband isotropic diamagnetic response and an all-angle negative index of refraction

SU XU,[1,4] JIAN-BIN LIU,[1,2] HAO WANG,[1] CI-KANG SU,[1] AND HONG-BO SUN[1,3,5]

[1]State Key Laboratory of Integrated Optoelectronics, College of Electronic Science and Engineering, Jilin University, Changchun 130012, China
[2]College of Physics, Jilin University, Changchun 130012, China
[3]State Key Laboratory of Precision Measurement Technology and Instruments, Department of Precision Instrument, Tsinghua University, Haidian, Beijing 100084, China
[4]e-mail: xusu@jlu.edu.cn
[5]e-mail: hbsun@tsinghua.edu.cn

Received 16 October 2018; revised 26 December 2018; accepted 14 January 2019; posted 15 January 2019 (Doc. ID 347939); published 11 February 2019

Metamaterials (MMs) and photonic crystals (PhCs) exhibiting artificially engineered physical properties have been widely studied in the past decade. However, abnormal properties could only be proposed under a limited range of polarization and directions in most of the previous studies. It is still a challenge to realize an isotropic artificial material with multiple exotic electromagnetic properties. Here we report a three-dimensional metacrystal supporting full polarization and omni-directional incidence. The center-symmetric unit cell consists of non-resonant closed metallic loops on each surface of the dielectric cube. With the cross-scale dispersion engineering, the metacrystal can exhibit an isotropic diamagnetic response and an all-angle negative index of refraction simultaneously at the opposite sides of the MM-PhC transition region. An additional numerical analysis shows the good performance in terahertz and mid-infrared frequencies, which indicates its potential applications on multi-functional optical components with wide polarization-and-direction allowance.

https://doi.org/10.1364/OL.44.000927

Metamaterials (MMs) [1–3] and photonic crystals (PhC) [4] brought breakthroughs on novel electromagnetic and optical devices in the past decade, such as invisibility cloaks [5,6], absorbers [7,8], compact guiding components for surface plasmon polaritons [9–11], wireless energy transfer devices [12,13], and subwavelength imaging devices [14–16]. Either MMs or PhCs are composed of periodic structures, despite the fact that they have different physical insights regarding the electrical scales of unit cells. As long as the functional transition and switch between the MMs and the PhCs can be achieved, more degree of freedom could be adopted to design artificial media and their applications [17].

Today, most of the proposed MM/PhC-based devices can only achieve their functionalities in limited polarizations and directions due to the spatial anisotropy [18–21]. The major bottlenecks on the realization of three-dimensional (3D) isotropic artificial media are the fabrication technique limitation, the resonant loss, and the narrow allowance on the polarization and incident direction in complex structures [22–28]. With the recent progress on out-of-plane lithography [29,30], it is experimentally feasible to create metallic patterns on every face of the substrate cube, which may pave the way for optical meta-devices from anisotropy to isotropy. Besides the difficulty mentioned above, the method for achieving a magnetic response at high frequency would also influence the performance of meta-devices.

Here we present an experimental demonstration of novel 3D isotropic metacrystals. The metacrystal unit cell consists of concentric metallic loops on each surface of the hollow cubic substrate. The all-angle negative index of refraction and broadband isotropic magnetic response are realized simultaneously in a single metacrystal. As the physical governing models vary at the opposite sides of the MM-PhC transition region, the design method could be treated as the cross-scale dispersion engineering. Additional numerical simulations show that the proposed metacrystal could exhibit a notorious optical magnetic response and negative index of refraction over the terahertz and mid-infrared frequencies.

We start with the metacrystal design at microwave as a proof of concept, which is illustrated in Fig. 1. The unit cell is constructed by metallic closed loops on every surface of the F4B dielectric cube with relative permittivity of 2.55 and loss tangent of 0.0015 at 10 GHz. The outer radius and the width of the metallic closed loop are $r_o = 2.8$ mm and $w = 0.15$ mm, respectively. The periodicity of the unit cell is $P = 6$ mm along each direction.

To study the electromagnetic characteristics of a metacrystal, a plane wave is illuminated along the z direction. Two Bloch–Floquet ports in the z direction and unit-cell boundary conditions in the x and y directions are employed in the

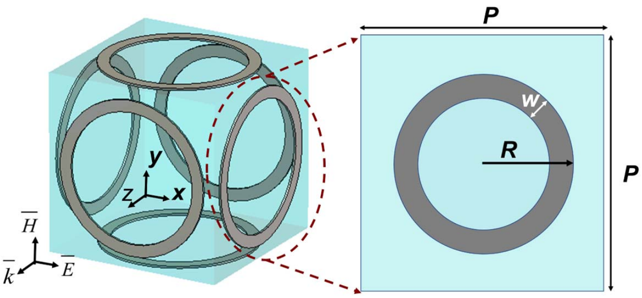

Fig. 1. Schematic of a metacrystal unit cell (left) and its planar geometrical property (right).

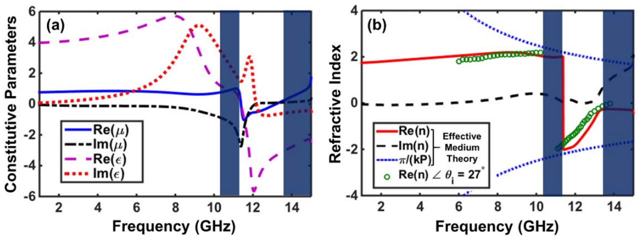

Fig. 2. Retrieval results of (a) constitutive parameters and (b) the refractive index for the metacrystal. In (b), a comparison of the refractive index retrieved from an effective medium theory under normal incidence and a far-field radiation pattern with an oblique incident angle $\theta_i = 27°$ was achieved.

simulation. Due to the fact that the metacrystal unit cell is center-symmetric, the electromagnetic isotropy is expected at a deep subwavelength scale. Through the retrieval results in Fig. 2(a), one can see that the real part of effective permeability is less than unity with little dispersion over the broad frequency range over 1 to 10 GHz which is far away from the first Brillouin zone [31]. When the frequency reaches the first Brillouin zone, the effective constitutive parameters vary rapidly. Figure 2(b) presents the refractive index and the first Brillouin zone. The negative index of refraction is retrieved from scattering parameters. The imaginary part of the permeability and refraction index at a low frequency range is close to zero, which is a desirable property for practical meta-device design. To verify the validity of the effective parameters closed to the first Brillouin zone and angular robustness, we adopt far-field radiation pattern method to calculate the real part of an effective refractive index. A piece of metacrystal wedge is used in the calculation. The shadow areas represent the frequency bands, where effective parameters extracted from the far-field radiation method are due to the markedly loss. One can see that the results via two methods agree well. Although the imaginary part of permeability shows negative values, it is still physically meaningful because the both the imaginary part of the refractive index and real part of impedance keep positive simultaneously, without violating energy conservation. Similar phenomena and physical mechanism were observed and discussed in Refs. [32–35] as well.

When frequency increases, the characteristics of the metacrystal could be converted from MMs to PhCs [17]. The k-surface analysis could be adopted to study the mechanism of negative refractive propagation for PhC materials. Figure 3(a) illustrates the band diagram of the metacrystal from 5 to 15 GHz.

The isofrequency contours of bands in the shadow region are plotted in Fig. 3(b) for the lower frequency region (e.g., from 10.5 to 11.5 GHz) and 3(c) for the higher region, respectively. One can see that there is a mixed frequency band in which the isofrequency contours are all convex [the shadow region of Fig. 3(a)]. As the frequency band is below the frequency $\omega < 0.5 \times 2\pi c/P$, the metacrystals could achieve an omni-directional negative refraction, according to the conditions that the isofrequency contours of the metacrystal are convex and larger than those of air [20,21]. In Fig. 4, we select the equal-frequency contours of 11.2 and 11.8 GHz in k surface as examples to show more information. Regarding the air-PhC interface shown in Fig. 4 in detail, the propagating modes with clear refractive characteristics could be determined by the conservation of frequency and the tangential components of the wave vector. As long as the contour is convex everywhere, waves from air could find a mode propagating into the metacrystal on the negative side of the interface. Note that the radius of isofrequency surfaces of the metacrystal should be larger than those of air. Otherwise, the propagating mode cannot be found, and an exponential attenuation of wave amplitudes will occur. Under such conditions, all-angle negative refraction could occur at the interface. The magnetic response and negative refraction rely on different dispersion management over the different electrically scale level. We treated this method as the cross-scale dispersion engineering.

Next, we fabricated a triangular metacrystal prism to verify the phenomena of the negative refraction in practice. The electrical field distribution refracted by a triangular metacrystal

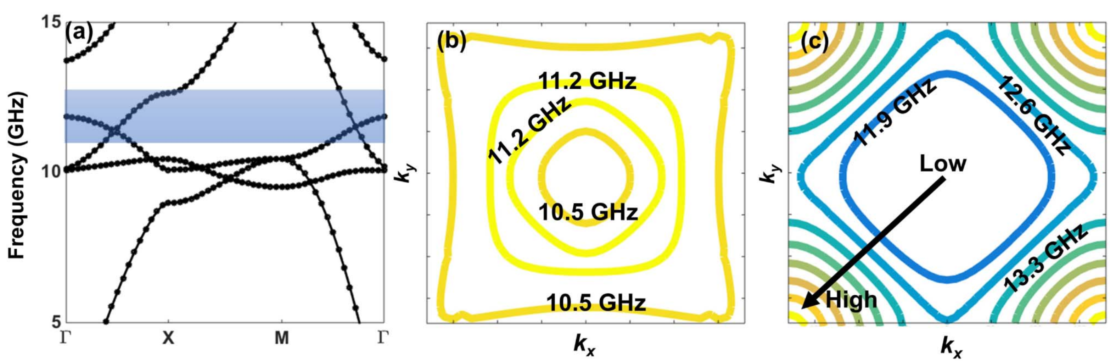

Fig. 3. Band structure analysis of the metacrystal. (a) Phase diagram, (b) the isofrequency contour of the lower band from 10.5 to 11.5 GHz, and (c) the isofrequency contour of a band higher than 11.5 GHz. The shadow region indicates the frequency band with a negative index of refraction.

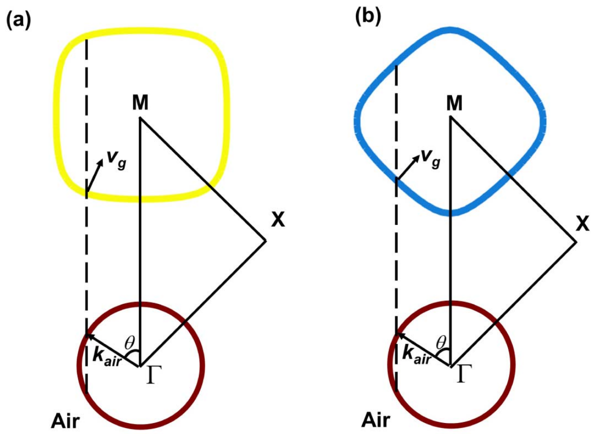

Fig. 4. Equal-frequency contours in k space of air and the metacrystals at (a) 11.2 and (b) 11.9 GHz are plotted, respectively, as examples. The waves encounter from the air to the metacrystal with the incident angle θ, and vg is the group velocity of the waves propagating in the metacrystal.

prism is measured in a parallel-plate waveguide, as shown in Fig. 5(a). The triangular prism consists of 21 × 11 × 3 unit cells along the x, y, and z directions, respectively. The metallic plates of the waveguides perform as a pair of electrical boundaries, which indicate the metacrystal sample with finite thickness could mimic infinite periodicity along the z direction. The incident wave is generated by a lens antenna. Absorbing materials are used to help the incident waves normally encounter onto the metacrystal prism at the position $x = 250$ mm. The electric field of the incident wave is along the z direction. To simplify the fabrication complexity, we fabricate the metacrystal with a comb-like dielectric holder in practice. The closed loops are printed on the wall of the comb, which is made of F4B substrate with the thickness of 0.5 mm. The numerical electrical field distributions of this triangular metacrystal prism are plotted at 8 and 12.5 GHz in Figs. 5(b) and 5(c), respectively. One can see that the metacrystal performs as a right-handed medium at 8.5 GHz, because the wave vectors of the refracted wave and incident wave lie at the opposite semi-space of the normal plane while, for the case of 12.5 GHz, the transmitted wave and incident wave occur at the same side of the normal plane, indicating that the metacrystal performs as a left-handed material.

The experimental transmitted electric field distribution was mapped with a LINBOU automatic 3D scanning platform, as shown in Figs. 5(d) and 5(e). The imaging plane in the experiment is marked as the white dashed–dotted line in Figs. 5(b) and 5(c), with the scanning area of 500 mm × 5 mm in the x–z plane. The scanning step width in the experiment is 1 mm in each direction. The positions of the refractive hotspots imaged by the probe at 8.5 and 12.5 GHz are marked by the red and yellow triangles, respectively. For the case of 8.5 GHz, as shown in Fig. 5(d), the transmitted beam and incident beam occur at the opposite semi-space separated by the normal plane. For the case of 12.5 GHz, as shown in Fig. 5(e), the transmitted beam is refracted to the same semi-space by the metacrystal prism. Therefore, the same negative refraction phenomena are observed in experiments as the simulation ones in Figs. 5(b) and 5(c). More simulation results of prism cases could be found in the online supplementary Visualization 1 and Visualization 2. Additionally, a 21 × 21 unit-cell square metacrystal matrix was adopted to verify the directional allowance of the metacrystal. The comb-like lattice is identical to the one shown in Fig. 5. The whole metacrystal matrix consists of 21 × 21 unit cells in the propagation plane. The excitation encounters onto the metacrystal matrix with the incident angles θ_i of 0 and 45 deg for the purpose of showing the all-angle backward wave supported by the metacrystal. The videos for the cases of normal incidence can be found in online supplementary Visualization 3 and Visualization 4, while Visualization 5 and Visualization 6 show the electrical field distributions under 45 deg oblique incidence. As the incident direction varies, the backward propagating wave could always be observed, which is the evidence on the all-angle negative index of refraction.

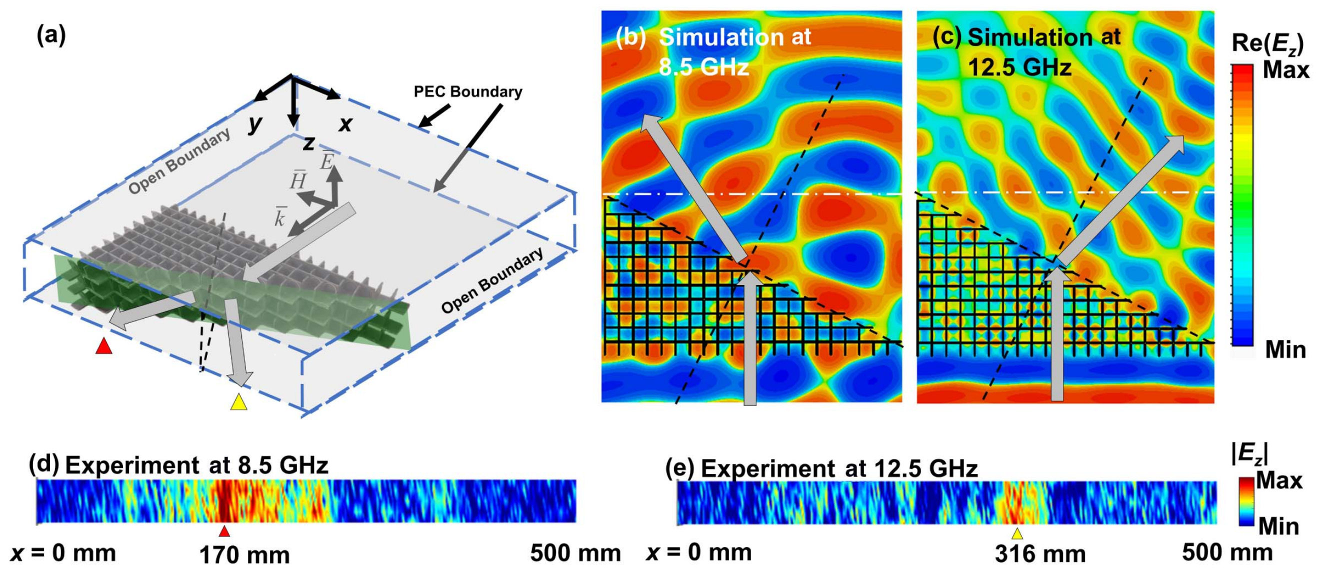

Fig. 5. Measurement of negative refraction. (a) Schematic of the experimental setup. The simulated electrical field distribution: (b) 8.5 and (c) 12.5 GHz. The experimental results of the triangular metacrystal prism: (d) 8.5 and (e) 12.5 GHz.

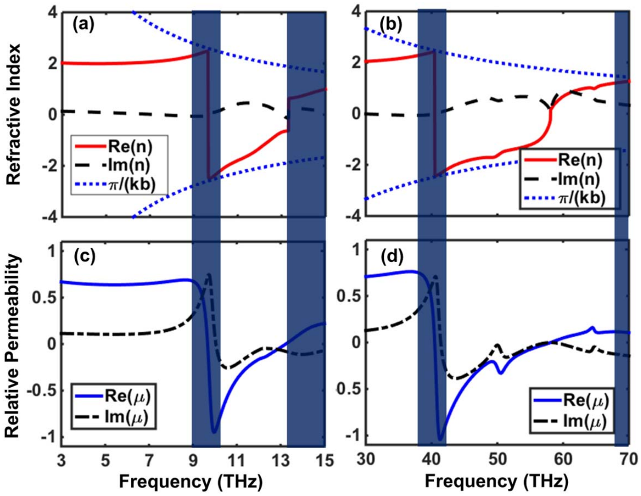

Fig. 6. Retrieved results of the metacrystal at the terahertz region (left column) and infrared frequencies (right column). (a) and (b) Refractive index. (c) and (d) Relative permeability. The metacrystals are scaled from the unit cell in Fig. 1 to 12.5 and 50 THz, respectively. The shadow regions shield the inaccurate results when the Brillouin zone is touched and where the absorbing ranges occur.

To explore the metacrystal performance at the terahertz and infrared regions, the periodicities of the unit cell for 12.5 and 50 THz are scaled from the geometry in Figs. 1 to 6 and 1.5 μm, respectively. The material of the closed loop used here is 0.1 μm thick gold, whose dispersion is determined with the plasma frequency of $2\pi \times 2.175 \times 10^{15}$ s^{-1} and collision frequency of $2\pi \times 6.5 \times 10^{12}$ s^{-1} [36]. The optical printing resist, SU-8, could be employed here as the supporting material. From the retrieval results shown in Fig. 6, one can see that the negative index refraction and broadband diamagnetic response could be achieved around 12.5 and 50 THz, respectively. Therefore, the metacrystal design is still functionally feasible in optical frequencies.

In conclusion, we have demonstrated a 3D metacrystal in both simulations and experiments. The diamagnetic response and negative index of refraction could be achieved in the same metacrystal structure simultaneously. Besides, the experimental demonstrations at microwaves, the practical feasibility at optical frequencies has been proved as well. Such multiple functional electromagnetic properties rely on different physical models between the MM and PhC. This functional realization, which is based on different dispersion management over the different electrical scale levels, could be treated as the cross-scale dispersion engineering. This Letter provides convincing evidence on the application of cross-scale dispersion engineering for the design and integration of multi-functional meta-structures and meta-devices with wide polarization-and-direction allowance.

Funding. National Natural Science Foundation of China (NSFC) (61805097, 21473076, 61435005S.X, 61590930, 61605055); National Key R&D Program of China (2017YFB1104300).

REFERENCES

1. H. Chen, J. Mater. Chem. **21**, 6452 (2011).
2. D. R. Smith, J. B. Pendry, and M. C. K. Wiltshire, Science **305**, 788 (2004).
3. C. M. Soukoulis and M. Wegener, Nat. Photonics **5**, 523 (2011).
4. J. D. Joannopoulos, S. G. Johnson, J. N. Winn, and R. D. Meade, *Photonic Crystals: Molding the Flow of Light*, 2nd ed. (Princeton University, 2008).
5. F. Sun, B. Zheng, H. Chen, W. Jiang, S. Guo, Y. Liu, Y. Ma, and S. He, Laser Photonics Rev. **11**, 1700034 (2017).
6. D. Schurig, J. J. Mock, B. J. Justice, S. A. Cummer, J. B. Pendry, A. F. Starr, and D. R. Smith, Science **314**, 977 (2006).
7. C. M. Watts, X. Liu, and W. J. Padilla, Adv. Mater. **24**, 98 (2012).
8. C. Zhang, Q. Cheng, J. Yang, and T.-J. Cui, Appl. Phys. Lett. **110**, 143511 (2017).
9. S. Xu, H. Xu, H. Gao, Y. Jiang, F. Yu, J. D. Joannopoulos, M. Soljacic, H. Chen, H. Sun, and B. Zhang, Proc. Natl. Acad. Sci. USA **112**, 7635 (2015).
10. F. Gao, Z. Gao, X. Shi, Z. Yang, X. Lin, H. Xu, J. D. Joannopoulos, M. Soljacic, H. Chen, L. Lu, Y. Chong, and B. Zhang, Nat. Commun. **7**, 11619 (2016).
11. F. Gao, H. Xue, Z. Yang, K. Lai, Y. Yu, X. Lin, Y. Chong, G. Shvets, and B. Zhang, Nat. Phys. **14**, 140 (2018).
12. A. Kurs, A. Karalis, R. Moffatt, J. D. Joannopoulos, P. Fisher, and M. Soljacic, Science **317**, 83 (2007).
13. M. Song, P. Belov, and P. Kapitanova, Appl. Phys. Rev. **4**, 021102 (2017).
14. I. M. Ehrenberg, S. E. Sarma, and B.-I. Wu, J. Appl. Phys. **112**, 073114 (2012).
15. S. Xu, Y. Jiang, H. Xu, J. Wang, S. Lin, H. Chen, and B. Zhang, Sci. Rep. **4**, 5212 (2014).
16. J. Sun, M. I. Shalaev, and N. M. Litchinitser, Nat. Commun. **6**, 7201 (2015).
17. M. V. Rybin, D. S. Filonov, K. B. Samusev, Y. S. K. Pavel, A. Belov, and M. F. Limonov, Nat. Commun. **6**, 10102 (2015).
18. J. B. Pendry, A. J. Holden, W. J. Stewart, and I. Youngs, Phys. Rev. Lett. **76**, 4773 (1996).
19. R. A. Shelby, D. R. Smith, and S. Schultz, Science **292**, 77 (2001).
20. C. Luo, S. G. Johnson, and J. D. Joannopoulos, Phys. Rev. B **65**, 201104 (2002).
21. C. Kubukcu, K. Aydin, E. Ozbay, S. Foteinopoulou, and C. M. Soukoulis, Nature **423**, 604 (2003).
22. J. D. Baena, L. Jelinek, and R. Marqués, Phys. Rev. B **76**, 245115 (2007).
23. L. Jelinek, R. Marqués, F. Mesa, and J. D. Baena, Phys. Rev. B **77**, 205110 (2008).
24. K. Hur, Y. Francescato, V. Giannini, S. A. Maier, R. G. Hennig, and U. Wiesner, Angew. Chem. Int. Ed. **50**, 11985 (2011).
25. D. Wu, S. Jiang, Y. Cheng, and X. Liu, Opt. Express **21**, 1076 (2013).
26. D. Güney, T. Koschny, and C. M. Soukoulis, Opt. Express **18**, 12348 (2010).
27. J. Q. Shen, Appl. Phys. Lett. **101**, 181002 (2012).
28. A. Grbic and G. V. Eleftheriades, J. Opt. **98**, 043106 (2005).
29. D. B. Burckel, J. R. Wendt, G. A. T. Eyck, J. C. Ginn, A. R. Ellis, I. Brener, and M. B. Sinclair, Adv. Mater. **22**, 5053 (2010).
30. A. Ishikawa and T. Tanaka, IEEE J. Sel. Top. Quantum Electron. **19**, 4700110 (2013).
31. X. Chen, T. M. Grzegorczyk, B.-I. Wu, J. J. Pacheco, and J.-A. Kong, Phys. Rev. E **70**, 016608 (2004).
32. T. Koschny, P. Markos, D. R. Smith, and C. M. Soukoulis, Phys. Rev. E **68**, 065602 (2003).
33. X. L. Shi, M. S. Cao, J. Yuan, and X. Y. Fang, Appl. Phys. Lett. **95**, 163108 (2009).
34. V. A. Markel, Phys. Rev. E **78**, 026608 (2008).
35. C. A. Dirdal and J. Skaar, Eur. Phys. J. B **91**, 131 (2018).
36. S. Linden, C. Enkrich, M. Wegener, J. Zhou, T. Koschny, and C. N. Soukoulis, Science **306**, 1351 (2007).